DOI: 10.26599/FSHW.2026.9251344

Contents lists available at SciOpen

Food Science and Human Wellness

journal homepage: https://www.sciopen.com/journal/2097-0765

China Food Publishing Co.

Carbon Source Substitution During Submerged Fermentation Alters *Cordyceps militaris* Extracellular Vesicle Metabolite Profiles and Anti-Photoaging Activity

Pengfei Li[a], Yujie Wang[a], Yue Wu[a], Guangzhao Wang[a], Ling Yan[c], Shiqi Lu[a], Junyi Wang[a], Wenfeng Liu[a], Kangliang Sheng[a,b,*], Yongzhong Wang[a,*]

[a] *School of Life Sciences and Medical Engineering, Key Laboratory of Human Microenvironment and Precision Medicine of Anhui Higher Education Institutes, Anhui University, Hefei 230601, Anhui, China*

[b] *Bengbu Medical University Affiliated Tongling Hospital. No.468 of Bijiashan Road. Tongguan District, tongling City, 244000, Anhui Province, China.*

[c] *School of Food and Biological Engineering, Hefei University of Technology, Hefei 230009, China*

ABSTRACT: Background: Cordyceps militaris extracellular vesicle-enriched preparations, operationally designated CMEVs in this study, are being explored as food-derived nanomaterials, but the effects of source material, fermentation stage, and carbon source on their characteristics and biological activity remain unclear. We compared CMEVs obtained from fruiting bodies and submerged liquid fermentation, selected a collection time, and examined the effects of four carbon sources on CMEV characteristics and protection against UVB-induced injury.

Results: Compared with fruiting body-derived CMEVs, fermentation-derived CMEVs yielded more BCA-detectable protein per gram of source dry mass, had a more negative zeta potential, and showed a narrower particle-size distribution. In UVB-damaged HaCaT cells, fermentation-derived CMEVs resulted in higher cell viability, lower *MMP1* and *IL6* expression, and higher *COL1A2* expression. The two source groups had similar particle-to-protein ratios. Although the BCA-measured protein concentration was highest on fermentation day 5, CMEVs collected on day 4 had a higher particle-to-protein ratio and a more uniform particle-size distribution. Day 4 was therefore selected for the subsequent experiments. Tre-CMEVs and Glc-CMEVs had similar protein concentrations, particle-to-protein ratios, and zeta potentials, while Tre-CMEVs showed a relatively narrow particle-size distribution. In UVB-damaged HaCaT cells, Tre-CMEVs reduced ROS and MDA, decreased *IL6* and *MMP1* expression, and increased *COL1A2* expression. Tre-CMEVs also reduced wrinkle formation, epidermal thickening, lipid peroxidation, inflammation, and collagen loss in UVB-exposed mice. Untargeted metabolomics distinguished Tre-CMEVs from Glc-CMEVs and identified differential features related to amino acid and energy metabolism, including signals putatively annotated as arginine, glutamate, and tricarboxylic acid-cycle intermediates.

Conclusions: Day 4 was selected as the collection point based on particle characteristics and cellular activity. Tre-CMEVs reduced oxidative stress, inflammatory responses, and matrix damage in HaCaT cells and alleviated UVB-induced skin injury in mice. These findings support further evaluation of Tre-CMEVs as a UVB-protective preparation.

Keywords: *Cordyceps militaris*; extracellular vesicle-enriched preparations; trehalose; UVB-induced photoaging

***Corresponding author**
Kangliang Sheng, kangliang@ahu.edu.cn;
Yongzhong Wang, yzwang@ahu.edu.cn

Received 26 May 2026
Received in revised from 27 July 2026
Accepted 3 September 2026

1. Introduction

Cordyceps militaris is an edible and medicinal fungus used in functional foods, dietary supplements, and traditional medicine[1, 2]. Its fruiting bodies and mycelia contain cordycepin, adenosine, ergosterol, polysaccharides, and other constituents with reported anti-inflammatory, antioxidant, and skin-protective activities[1-3]. Submerged liquid fermentation provides a controllable means of producing *C. militaris* biomass and bioactive products[4, 5]. Nutrient composition and cultivation conditions strongly influence fungal growth and cordycepin production[6-8]. Fermentation can also alter the properties of mushroom polysaccharides[9] and other food-derived bioactive components[10]. Whether these variables similarly affect C. militaris extracellular vesicle-enriched preparations, operationally designated CMEVs in this study, has not been established.

Extracellular vesicles (EVs) are nanoscale lipid-bilayer particles that transport proteins, lipids, small RNAs, and metabolites between cells and across biological kingdoms[11-13]. Fungal EV studies indicate that vesicles carry proteins, RNAs, lipids, glycans, and metabolites and may participate in growth, stress adaptation, host interaction, and intercellular communication[14-16]. EVs from plants, fermented foods, and edible or medicinal fungi have attracted interest as food-derived nanocarriers because they combine biocompatibility, scalable raw materials, and endogenous cargo delivery potential[17-23]. Shiitake mushroom-derived extracellular nanovesicles have been investigated for controlled preparation, characterization, and in vitro activity[24], while related vesicle-like nanoparticles have subsequently been evaluated in aged-mouse dietary intervention models[25]. EVs from *Pleurotus eryngii* have also been described as antioxidant mushroom-derived vesicles[26]. Fungal and plant-derived exosome-like nanovesicles have also been investigated for ultraviolet-induced skin aging and skin-directed anti-aging delivery[27-29].

The composition of EV preparations depends on the physiological and metabolic state of the producer cells[14-16]. In filamentous fungi, culture conditions alter particle size and protein composition[30]. Carbon source is particularly relevant in *C. militaris* because it affects both mycelial growth and secondary metabolism[3-5]. Trehalose can serve as a carbon source and also contributes to fungal stress protection, cell-wall homeostasis, and metabolic regulation through the trehalose/trehalose-6-phosphate pathway[31, 32]. We therefore examined whether replacing glucose with trehalose or other carbon sources altered CMEV characteristics and activity.

Source material and collection time may also influence CMEV preparations. Fruiting bodies are differentiated tissues rich in structural polysaccharides and tissue-associated metabolites, whereas submerged liquid fermentation releases vesicular material into a broth in which growth, pH, nutrient composition, and harvest time can be monitored. A previous study reported exosome-like nanovesicles from *C. militaris* fruiting bodies[33], but fruiting body-derived and fermentation-derived CMEVs have not been directly compared. The stage of fermentation at which CMEVs should be collected also remains unclear.

In this study, we first compared CMEVs obtained from fruiting bodies and glucose-based submerged liquid fermentation. We then selected the collection day by integrating mycelial growth, particle characteristics, and activity in UVB-damaged HaCaT cells. Next, we compared CMEVs produced with

glucose, trehalose, galactose, or glycerol. Untargeted metabolomics was used to compare Tre-CMEVs with Glc-CMEVs, and Tre-CMEVs identified through the in vitro screening were subsequently evaluated in a mouse model of UVB-induced photoaging.

2. Materials and methods

2.1. Strain, cells, and animals

The *Cordyceps militaris* strain HMJAU 25074 was identified by internal transcribed spacer sequencing and maintained by routine laboratory subculture. Human immortalized keratinocytes (HaCaT; STCC11801, Wuhan Zishan Biotechnology Co., Wuhan, China) were cultured in DMEM-H medium (Servicebio, Wuhan, China) supplemented with 10% fetal bovine serum and 1% penicillin/streptomycin at 37 °C in 5% CO_2. Cells were passaged after digestion with 0.25% trypsin-EDTA at 37 °C for 5–6 min and subcultured at a 1:3 ratio. Mycoplasma testing was negative.

Seven-week-old female SPF-grade ICR mice (20 ± 2 g) were supplied by Hefei Qingyuan Biotechnology Co., Ltd. (Hefei, China) and produced by Hangzhou Ziyuan Laboratory Animal Technology Co., Ltd. (Hangzhou, China; laboratory animal production license No. SCXK (Zhe) 2024-0004; laboratory animal quality certificate No. 20250922Abzz010500000083). Animals were housed under standard SPF conditions at 18–22 °C and 45–65% relative humidity under a 12 h light/dark cycle, with free access to standard chow and sterilized water. All animal procedures were approved by the authors' Institutional Animal Care and Use Committee (No. IACUC(AHU)-2025-111) and conducted in accordance with the ARRIVE 2.0 guidelines[34].

2.2. Reagents and instruments

Major reagents, assay kits, and instruments used in this study are listed in Additional file 1: Table S4, together with their suppliers and intended uses.

2.3. Submerged liquid fermentation and kinetic monitoring

The basal medium contained the assigned carbon source, yeast extract (5 g/L), $MgSO_4$ (0.4 g/L), KH_2PO_4 (0.6 g/L), and vitamin B1 (0.01 g/L). The carbon sources were adjusted to an equivalent carbon concentration of approximately 0.546 mol C/L: glucose, 16.4 g/L; galactose, 16.4 g/L; trehalose, 15.56 g/L; and glycerol, 16.76 g/L.

Activated *C. militaris* cultures were inoculated into fermentation medium at 10% (v/v) and incubated at 22.7 °C and 170 rpm for 1-9 days. Samples were collected daily for biomass monitoring. Mycelia were harvested by filtration, washed with PBS, and analyzed by dry-weight measurement. Initial broth pH and the pH at the peak-biomass-phase collection point were recorded for each carbon-source condition. Glc-CMEVs, Tre-CMEVs, and Gal-CMEVs were collected on day 4, whereas Gly-CMEVs were collected on day 5. These time points corresponded to the condition-specific peak-biomass phase. For each carbon-source condition, three independent shake-flask submerged liquid fermentation batches were independently inoculated, fermented, harvested, and subjected to the complete CMEV enrichment procedure; therefore, n = 3 denotes independent biological preparation batches rather than technical replicates from one preparation.

2.4. Preparation of CMEVs from fruiting bodies and fermentation broth

Materials recovered from *C. militaris* using the enrichment procedure described below are referred to as CMEVs. This term denotes extracellular vesicle-enriched preparations and does not imply a fully purified vesicle population.

Unless otherwise specified, FB-CMEVs and SF-CMEVs were subjected to the same downstream enrichment, washing, physicochemical characterization, and HaCaT-cell bioassay workflow. These operational group labels were used for the source-comparison experiment. In the subsequent carbon-source experiments, glucose-, trehalose-, galactose-, and glycerol-derived submerged liquid fermentation preparations were abbreviated as Glc-CMEVs, Tre-CMEVs, Gal-CMEVs, and Gly-CMEVs, respectively. The difference between FB-CMEVs and SF-CMEVs was restricted to the source pretreatment step; after clarification by filtration, both source materials were subjected to the same centrifugation, DTT-mediated release, PEG enrichment, washing, and PBS resuspension procedure.

For the source comparison, the dry weight of the fruiting-body material was determined from a parallel aliquot of the same batch after drying to constant weight, whereas the denominator for SF-CMEVs was the dry mycelial biomass obtained from the corresponding fermentation batch. Protein recovery was calculated by dividing the total BCA-measured protein recovered from each preparation by the corresponding source dry mass. This normalization was used as an operational source-specific comparison and does not imply that fruiting-body tissue and mycelial biomass are biologically equivalent matrices.

The clarified fruiting-body filtrate or fermentation broth was centrifuged at 5000 × *g* for 25 min at 4 °C to remove residual large debris. The supernatant was further centrifuged at 15000 × *g* for 20 min at 4 °C to generate supernatant S1 and a pellet fraction. The pellet was resuspended in prechilled isolation buffer containing sucrose (3.43 g) and triethanolamine (149 μL) in water to a final volume of 50 mL. DTT was added to a final concentration of 0.15 g/mL, and the suspension was incubated at 37 °C for 12 min as a matrix-dissociation step, with reference to a previously reported DTT-assisted extraction procedure[35]. The mixture was immediately diluted with two volumes of isolation buffer and centrifuged at 17000 × g for 25 min at 4 °C to obtain supernatant S2.

S1 and S2 were combined, and PEG 8000 was added to a final concentration of 8% (w/v). After mixing, samples were incubated overnight at 4 °C and centrifuged at 18000 × *g* for 70 min at 4 °C. The pellet was collected as a crude EV-enriched preparation, resuspended in sterile PBS, washed once by centrifugation at 18000 × *g* for 30 min at 4 °C, and finally resuspended in sterile PBS. Samples were used for physicochemical characterization and biological assays or stored at −80 °C. This workflow combines differential centrifugation, DTT-mediated release, polymer-mediated enrichment, and PBS washing; it is therefore described as an EV enrichment procedure rather than as single-step PEG precipitation or fully purified EV isolation[11, 36, 37]. This terminology follows MISEV2023 guidance for EV preparations that may contain coisolated nonvesicular components[11, 12]. Recent guidance for EV extraction from edible sources also stresses transparent reporting of source-dependent pretreatment, isolation, and characterization[38].

2.5. DTT-step evaluation, process controls, and batch reproducibility

To evaluate the contribution of the DTT step, independent DTT-treated (DTT+) and DTT-free (DTT−) preparations were generated from separate starting samples and processed under otherwise identical conditions, including dilution, centrifugation, PEG enrichment, washing, resuspension, and physicochemical analysis. Each group comprised three independently prepared and fully processed samples. Intensity-weighted particle-size distributions, zeta potential, and BCA-measured protein concentration were compared between the two groups. This comparison assessed detectable changes in particle-size distribution, surface charge, and protein recovery; it did not directly evaluate membrane integrity, molecular composition, residual DTT, or particle-normalized biological activity.

Two types of full-process negative controls were prepared. Complete Glc-, Tre-, Gal-, and Gly-containing media without *C. militaris* inoculation were processed using the same starting volume, DTT treatment, PEG concentration, centrifugation, washing, and final resuspension volume as the biological samples. A DTT treatment and PEG enrichment process blank containing the processing buffers and reagents but no fermentation medium or biological material was processed in parallel. Each control condition comprised three independently prepared and fully processed replicates. The resulting controls were evaluated by intensity-weighted particle-size analysis, zeta-potential measurement, and BCA protein assay; results below the assay quantification range were reported as below the lower limit of quantification rather than as zero.

Batch-to-batch reproducibility was assessed using three independently inoculated, fermented, harvested, and processed batches for each carbon-source condition. BCA-measured protein concentration, particle size, and zeta potential were summarized as mean ± SD and coefficient of variation. Functional consistency among the three independently prepared Tre-CMEV batches was additionally evaluated in UVB-injured HaCaT cells using MDA accumulation as the readout.

2.6. Physicochemical characterization

The morphology of CMEVs was examined by TEM. Briefly, 20 μL of each preparation in PBS was applied to glow-discharged carbon-coated copper grids, negatively stained with 2% phosphotungstic acid, and imaged with a Talos L120C G2 TEM. Intensity-weighted particle-size distributions and zeta potentials were measured using light-scattering analysis under matched settings. NTA was used separately to obtain size-resolved particle-concentration profiles and total particle concentrations[39]. Total protein was quantified with a BCA assay. The particle-to-protein ratio was calculated as total NTA-detectable particle concentration (particles/mL) divided by BCA-measured protein concentration (μg/mL) and is reported as particles/μg protein. Cell and animal doses were normalized to BCA-measured total protein; this does not constitute particle-number normalization. Particle measurements also do not establish that every detected particle is an EV or exclude co-enriched nonvesicular material[11, 36, 37].

2.7. Cellular uptake, UVB-induced cell injury, and in vitro efficacy assays

For cellular uptake analysis, CMEVs were fluorescently labeled with DiI according to the manufacturer's protocol. Excess free dye was removed by centrifugation and washing before cell treatment. A processed DiI-only control was prepared by adding DiI to the same labeling buffer in the absence of CMEVs and subjecting it to the same dye concentration, incubation time, buffer volume, centrifugation, washing, and final resuspension procedure. HaCaT cells were treated with DiI-labeled preparations or the processed DiI-only control using the same treatment volume and incubation time. DiI-labeled CMEVs were applied at 100 μg/mL for 12 h. After incubation, cells were washed with PBS, nuclei were counterstained with DAPI, and fluorescence images were acquired using identical laser power, detector gain, exposure, magnification, and image-processing settings.

HaCaT cells in logarithmic growth phase were used for in vitro experiments. For biocompatibility assays, approximately 8000 cells per well were seeded into 96-well plates and allowed to adhere for 24 h. CMEVs were added at 20, 40, or 60 μg/mL and incubated for 24 h. CCK-8 reagent was then added, cells were incubated in the dark for approximately 3 h, and absorbance was read at 450 nm. Cell viability was normalized to the untreated control.

For the UVB injury model, HaCaT cells were exposed to UVB irradiation on two consecutive days. The UVB dose was 40 mJ/cm² on day 1 and 50 mJ/cm² on day 2 using UVB-313 nm fluorescent lamps, with emission mainly within 280–315 nm. UVB models are widely used to induce oxidative stress, inflammatory signaling, extracellular-matrix dysregulation, and collagen loss in photoaging research[40-42]. Immediately after the second UVB exposure, cells were treated with the corresponding CMEVs at 50 μg/mL, normalized according to BCA-measured total protein, for 24 h. Model cells received an equal volume of PBS without CMEVs. This two-step UVB exposure protocol established an accelerated photodamage model before post-irradiation CMEVs intervention.

2.8. ROS, MDA, and image quantification

Intracellular ROS was detected with DCFH-DA. After intervention, cells were gently washed with PBS, incubated with DCFH-DA working solution diluted in serum-free medium at 37 °C for 20 min in the dark, and washed three times with PBS to remove free probe. Fluorescence images were acquired under identical exposure settings, and mean fluorescence intensity was quantified with ImageJ. Lipid peroxidation was assessed with an MDA assay based on thiobarbituric acid according to the manufacturer's instructions, with normalization performed as required by the kit protocol.

2.9. Untargeted metabolomics

Glc-CMEVs and Tre-CMEVs were obtained from three independent fermentation and complete CMEV-enrichment batches per group for untargeted metabolomics. Each replicate originated from an independently inoculated fermentation and complete CMEV-enrichment batch. Metabolites were extracted with methanol/acetonitrile (1:1, v/v) in a total extraction volume of 390 μL. Samples were sonicated at 40 kHz for 35 min at 5 °C and incubated at −40 °C for 40 min to promote protein precipitation. After centrifugation at 12000 × g for 16 min at 4 °C, supernatants were transferred to fresh tubes and dried under a gentle nitrogen

stream. Dried extracts were reconstituted in 110 μL of acetonitrile/water (1:1, v/v), briefly sonicated at 5 °C, centrifuged again at 12000 × g for 16 min at 4 °C, and transferred to vials for LC-MS/MS analysis. Untargeted metabolomics was treated as a discovery workflow rather than as proof of molecular causality[43].

Metabolomics was performed with a Thermo Fisher Scientific UHPLC system coupled to a Q Exactive quadrupole-Orbitrap mass spectrometer. Separation used an HSS T3 column with a 2 μL injection volume and a flow rate of 0.39 mL/min. Mobile phase A was water/acetonitrile (95:5, v/v) with 0.1% formic acid, and mobile phase B was acetonitrile/isopropanol/water (47.5:47.5:5, v/v/v) with 0.1% formic acid. The gradient was as follows: 0–0.11 min, 0–5% B; 0.11–2.1 min, 5–25% B; 2.1–9.1 min, 25–100% B; 9.1–13.1 min, 100% B; 13.1–13.2 min, 100–0% B; and 13.2–16.1 min, 0% B for re-equilibration. Samples were kept at low temperature in the autosampler.

Electrospray ionization was performed in positive and negative modes. Source parameters were heater temperature, 400 °C; capillary temperature, 320 °C; sheath gas, 40 arbitrary units; auxiliary gas, 10 arbitrary units; spray voltage, 3500 V in positive mode and −2800 V in negative mode. MS/MS collision energies were 20, 40, and 60 eV. Full MS and MS/MS resolutions were 70000 and 17500, respectively. Data were acquired in data-dependent acquisition mode across m/z 70–1050. Raw data were processed for peak detection, alignment, denoising, missing value handling, and normalization. Metabolite names and chemical classifications were reported using RefMet terminology where available[44], and pathway mapping was performed using KEGG[45]. OPLS-DA was used to visualize global metabolic separation, with permutation testing for model stability. Differential features were screened using VIP > 1.0 from OPLS-DA combined with a Benjamini–Hochberg-adjusted $P < 0.05$. Metabolite annotations were reported as putative annotations unless confirmed with authentic standards[46].

Auxiliary metabolomic comparisons of Tre-CMEVs with Gal-CMEVs and Gly-CMEVs used the same LC-MS/MS processing pipeline as the primary Tre-CMEVs versus Glc-CMEVs comparison. The corresponding OPLS-DA score plots and VIP-associated heat maps are provided in Additional file 1: Figure S6.

2.10. Mouse UVB photoaging model and Tre-CMEVs intervention

After acclimation, mice were randomly assigned to three groups (n = 6): Control, UVB Model, and Tre-CMEVs. The animal experiment was designed as a proof-of-concept validation following the in vitro carbon-source screening. Tre-CMEVs were selected as the lead preparation based on their overall physicochemical characteristics and protective responses in UVB-injured HaCaT cells. This staged screening-to-validation design limited animal use to the selected candidate and was consistent with the Reduction principle of the 3Rs. Dorsal hair was removed before modeling, and the exposed area was kept consistent throughout the experiment. A continuous 14-day UVB protocol was used. The dose was 100 mJ/cm² on day 1 and was increased by 50 mJ/cm² every 3 days for 2 weeks. Repeated UVB exposure induces erythema, epidermal hyperplasia, oxidative injury, inflammatory activation, and dermal collagen remodeling in experimental photoaging models[40-42, 47]. Before each irradiation, mice in the Tre-CMEVs group received a

subcutaneous injection of Tre-CMEVs into the dorsal irradiation area at 50 μg per mouse per treatment. Control and UVB Model mice received equal volumes of PBS. Dorsal erythema, scaling, and wrinkles were recorded during the experiment, and wrinkle severity was scored. At the endpoint, mice were euthanized according to the approved ethical protocol. Dorsal skin and major organs were collected, fixed, embedded, or stored at −80 °C according to downstream analyses.

For the preliminary in vivo tolerability assessment, body weight was monitored during the observation period. Major organs, including heart, liver, spleen, lung, kidney, and skin, were collected for H&E staining after Tre-CMEVs administration. These data are presented in Additional file 1: Figure S7.

2.11. Histology and gene expression analysis

Dorsal skin tissues were fixed in paraformaldehyde, embedded in paraffin, and sectioned at approximately 4 μm. Sections were stained with hematoxylin and eosin (H&E) or Masson's trichrome to assess epidermal thickness, keratinization, and dermal collagen distribution. Images were acquired at identical magnification and exposure settings. Epidermal thickness and dermal collagen area fraction were quantified with ImageJ.

For RT-qPCR, total RNA was extracted from cells or skin tissues with TRIzol reagent. RNA concentration and purity were measured before reverse transcription to cDNA. Real-time PCR was performed with a SYBR Green system, *GAPDH* served as the internal control, and relative mRNA expression was calculated by the $2^{-\Delta\Delta Ct}$ method. In HaCaT cells, RT-qPCR targeted *IL-6*, *MMP-1*, and *COL1A2*, with *GAPDH* as the internal reference gene. In mouse dorsal skin tissues, RT-qPCR targeted *IL-1β*, *MMP1A*, and *COL1A2*, also with *GAPDH* as the internal reference gene. Primer sequences are listed in Additional file 1: Table S3. Additional dorsal skin samples were homogenized for MDA measurement according to the assay kit protocol, and MDA values were normalized to the total protein concentration.

2.12. Statistical analysis

Data are presented as mean ± standard deviation (SD). GraphPad Prism 8.0 was used for statistical analysis. For physicochemical characterization, n = 3 denotes three independently prepared CMEV preparations or three independently fermented and fully processed batches, as specified. For cell assays, n = 3 denotes three independent cell experiments; technical replicate wells or fields were averaged within each independent experiment before inferential analysis. Metabolomics used three independent fermentation and preparation batches per group. Animal endpoints included six mice per group, with no missing endpoint samples. Normality and homogeneity of variance were evaluated using the Shapiro-Wilk and Brown-Forsythe tests, respectively; no statistically significant departure from these assumptions was detected for the analyzed datasets (all $P > 0.05$). Two-group comparisons between independently prepared groups were analyzed using an unpaired two-tailed Student’s t test. Multi-group comparisons were analyzed by one-way ANOVA followed by Dunnett's multiple-comparison test against the prespecified reference group: D4 for fermentation-stage characterization, Glc-CMEVs for carbon-source physicochemical comparisons, the UVB Model group for cell-intervention experiments, and the UVB Model group for the animal experiment. The

prespecified reference group, significance symbols, and corresponding thresholds are defined in each figure legend. Untargeted metabolomics used Benjamini-Hochberg-adjusted P values, with VIP > 1.0 and adjusted $P < 0.05$ used for differential-feature screening. $P < 0.05$ was considered statistically significant; $^{*}P < 0.05$, $^{**}P < 0.01$, and $^{***}P < 0.001$.

3. Results

3.1. CMEVs derived from submerged liquid fermentation and fruiting bodies show source-dependent differences

The enrichment workflow for FB-CMEVs and SF-CMEVs is shown in Figure 1A. The amount of protein recovered per gram of source dry mass, as measured by the BCA assay, was higher for SF-CMEVs than for FB-CMEVs (Figure 1B). TEM showed vesicle-like membranous particles in both groups, with less amorphous background and a more uniform morphology in the representative SF-CMEVs images (Figure 1C). SF-CMEVs also showed a more negative zeta potential and a narrower particle size distribution than FB-CMEVs (Figure 1D,E). The particle-to-protein ratio did not differ significantly between the two groups (Additional file 1: Figure S3A).

Control experiments showed that DTT-treated and DTT-free preparations had similar particle size distributions and zeta potentials, whereas DTT treatment increased the amount of protein recovered (Additional file 1: Figure S1). The uninoculated medium controls and the DTT treatment and PEG enrichment process blank showed only small-diameter scattering signals and low or unquantifiable protein levels after complete processing (Additional file 1: Figure S2).

To evaluate cellular uptake, DiI-labeled FB-CMEVs and SF-CMEVs were incubated with HaCaT cells for 12 h. Cells treated with DiI-labeled CMEVs showed prominent red fluorescence within the cytoplasmic region (Figure 1F), whereas the processed DiI-only control showed minimal fluorescence under identical acquisition settings (Additional file 1: Figure S5). These results support the uptake of DiI-labeled CMEVs by HaCaT cells and indicate that the observed fluorescence was not attributable to residual free dye or dye-derived aggregates. In UVB-injured HaCaT cells, both FB-CMEVs and SF-CMEVs increased cell viability compared with the UVB Model group, with a larger increase observed in the SF-CMEVs group (Figure 1G). Both treatments decreased *MMP-1* and *IL-6* mRNA expression and increased *COL1A2* mRNA expression, with more pronounced changes observed in the SF-CMEVs group (Figure 1H–J).

Based on these results, SF-CMEVs were used in the subsequent fermentation-stage and carbon-source experiments.

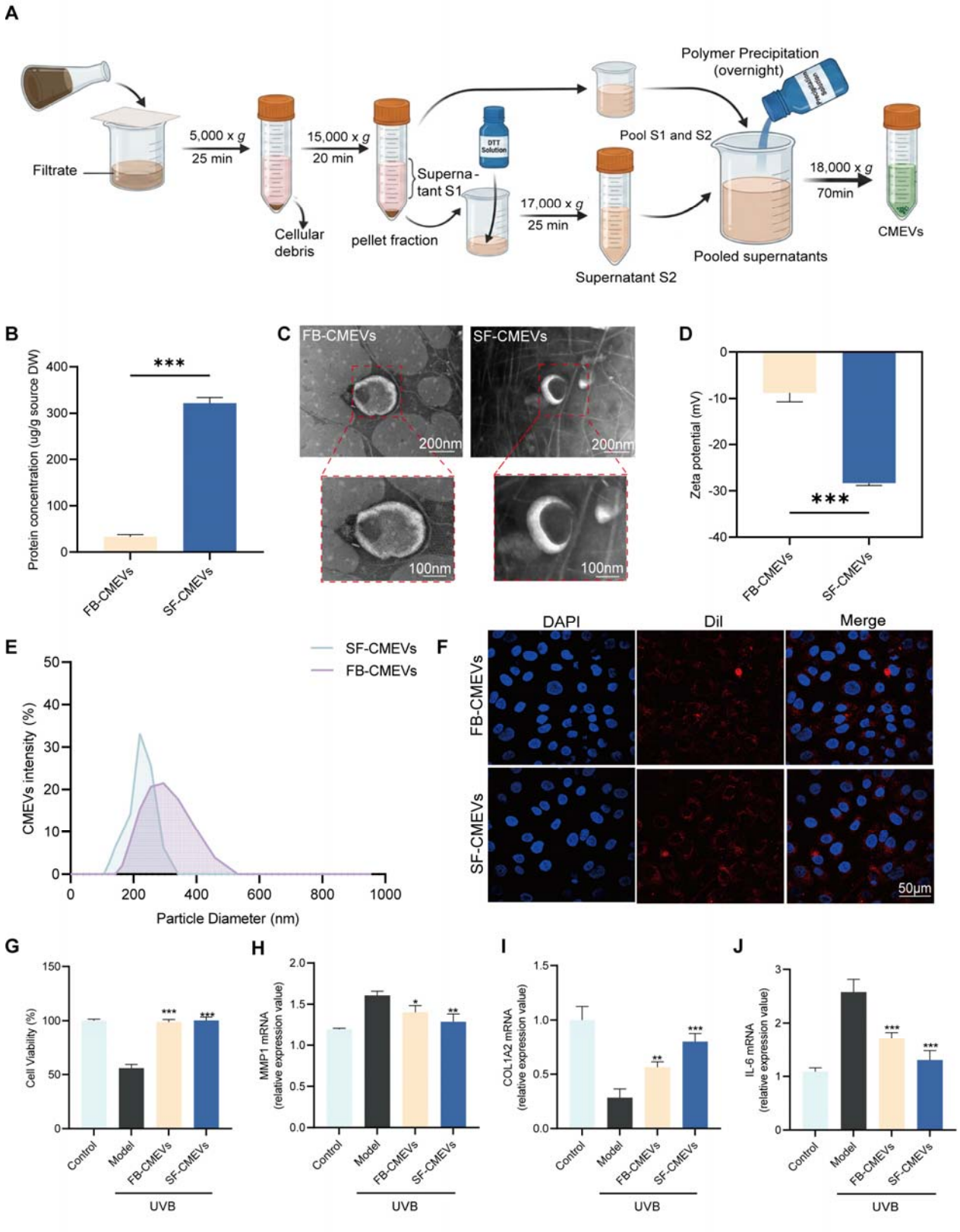


Figure 1. Source-dependent differences between FB-CMEVs and SF-CMEVs. (A) Schematic workflow for CMEV enrichment. (B) Protein recovered per gram of source dry mass, measured by the BCA assay. (C) Representative TEM images; scale bars, 200 nm and 100 nm. (D) Zeta potential. (E) Intensity-weighted particle-size distribution. (F) Cellular uptake of DiI-labeled FB-CMEVs and SF-CMEVs after 12 h incubation with HaCaT cells; nuclei were stained with DAPI. (G) Cell viability in UVB-damaged HaCaT cells. (H-J) Relative mRNA expression of *MMP1*, *COL1A2*, and *IL-6*. Physicochemical data are mean ± SD from three independent CMEV preparations; cell data are mean ± SD from three independent cell experiments. Physicochemical comparisons used an unpaired two-tailed Student's t test, and cell comparisons used one-way ANOVA with Dunnett's test against the UVB Model group. *$P < 0.05$, **$P < 0.01$, ***$P < 0.001$.

3.2. Fermentation day 4 was selected as the collection time for CMEVs

To determine the collection time, fermentation kinetics were examined using glucose as the carbon source. Mycelial biomass reached a maximum or plateau on fermentation day 4, while broth pH decreased and subsequently stabilized (Figure 2A). Protein concentration measured by the BCA assay increased from day 3 to day 4 and reached its highest level on day 5 (Figure 2D). However, CMEVs collected on day 5 had a lower particle-to-protein ratio than those collected on day 4, whereas the ratios on days 3 and 4 were comparable (Figure 2E). Thus, the increase in protein concentration on day 5 was not accompanied by a proportional increase in NTA-detectable particles.

The physicochemical profile also varied with growth stage. D4-CMEVs showed a relatively narrow intensity-weighted particle-size distribution and representative vesicle-like structures with a comparatively cleaner background (Figure 2B,F). D5-CMEVs showed a broader distribution extending toward larger particles, a less negative zeta potential than D4-CMEVs, and greater morphological heterogeneity in the representative TEM fields (Figure 2B,C,F). These observations are consistent with increased co-recovery of heterogeneous particulate and protein-containing material at the later collection stage, although the present measurements cannot distinguish vesicle-associated proteins from free or nonvesicular proteins.

Compared with the UVB Model group, CMEVs collected on day 4 reduced intracellular ROS and MDA levels, decreased *IL-6* and *MMP-1* mRNA expression, and increased *COL1A2* mRNA expression (Figure 3A–F). Based on the combined fermentation, physicochemical, morphological, and cellular results, fermentation day 4 was selected as the collection time for subsequent experiments.

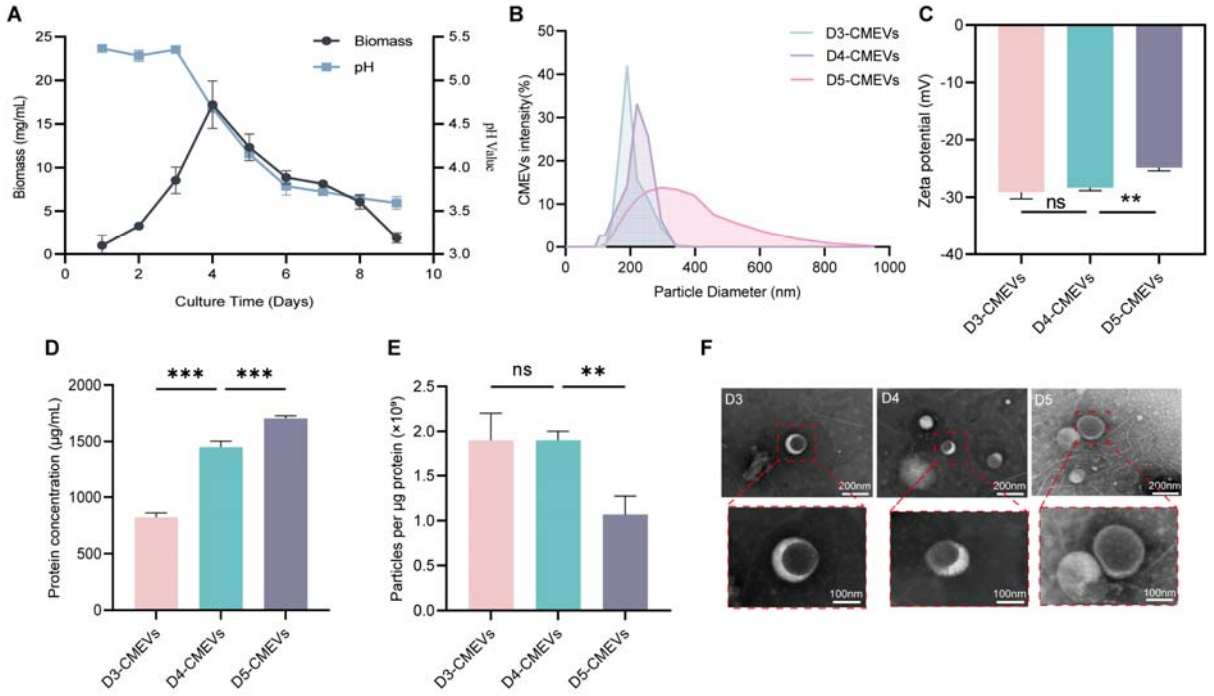


Figure 2. Effects of fermentation stage on CMEV characteristics. D3-CMEVs, D4-CMEVs, and D5-CMEVs denote CMEVs collected on fermentation days 3, 4, and 5, respectively. (A) Dynamic changes in mycelial biomass and broth pH during submerged liquid fermentation of *C. militaris*. (B) Intensity-weighted particle size distributions of CMEVs collected on fermentation days 3, 4, and 5. (C) Zeta potential. (D) BCA-measured protein concentration. (E) NTA-detectable particles per μg of BCA-measured protein. (F) Representative TEM images; upper scale bars, 200 nm; lower scale bars, 100 nm. Data are mean ± SD from three independent fermentation and complete preparation batches. Comparisons used one-way ANOVA with Dunnett's test using CMEVs collected on day 4 as the reference group. $^{**}P < 0.01$, $^{***}P < 0.001$, ns, not significant.

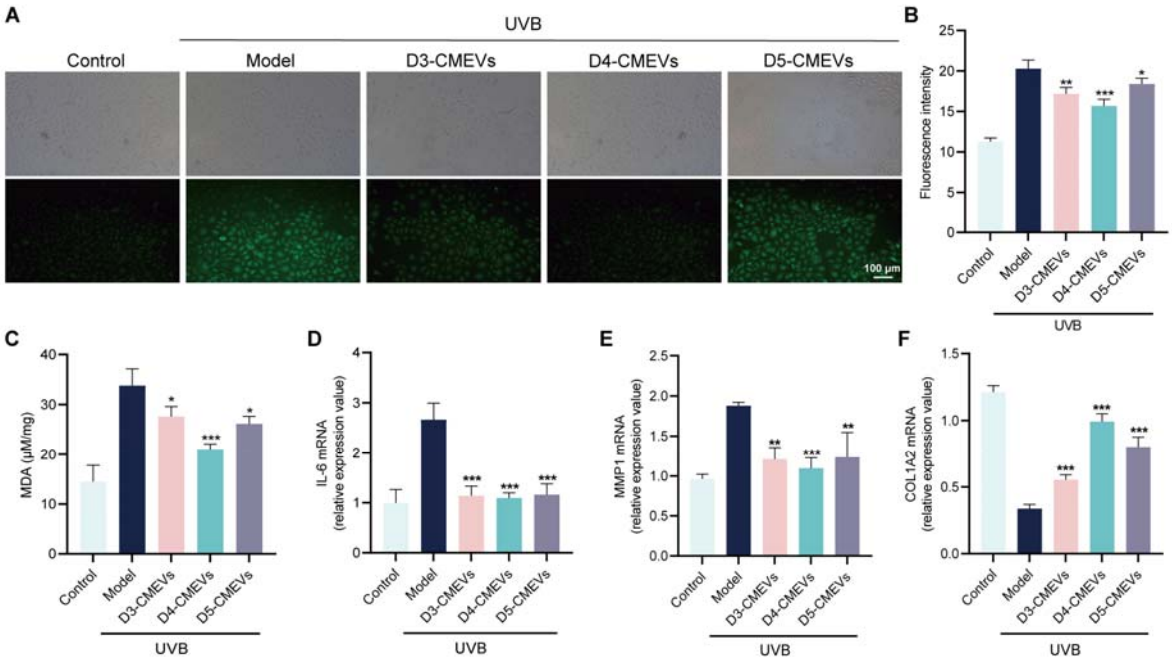


Figure 3. Protective effects of CMEVs collected at different fermentation stages against UVB-induced HaCaT cell injury. D3-CMEVs, D4-CMEVs, and D5-CMEVs denote CMEVs collected on fermentation days 3, 4, and 5, respectively. (A) Representative bright-field and DCFH-DA fluorescence images showing intracellular ROS accumulation. (B) Quantification of relative intracellular ROS fluorescence intensity. (C) Intracellular MDA concentration measured by a TBA-based assay. (D-F) Relative mRNA expression of *IL-6*, *MMP-1*, and *COL1A2*. Data are mean ± SD, n = 3. Statistical comparisons were made between each CMEV-treated group and the Model group by one-way ANOVA with Dunnett's post hoc test; *$P < 0.05$, **$P < 0.01$, ***$P < 0.001$.

3.3. Effects of carbon source on the physicochemical properties of CMEVs

Using the peak-biomass collection strategy, CMEVs produced with glucose, trehalose, galactose, or glycerol were compared. Glc-CMEVs, Tre-CMEVs, and Gal-CMEVs were collected on fermentation day 4, whereas Gly-CMEVs were collected on day 5. The four carbon-source conditions showed different biomass trajectories and changes in broth pH (Figure 4A,B).

Protein concentrations measured by the BCA assay differed among the four groups (Figure 4E). Gal-CMEVs and Gly-CMEVs had lower protein concentrations than Glc-CMEVs, whereas Tre-CMEVs did not differ significantly from Glc-CMEVs. The particle-to-protein ratios did not differ significantly among the four groups (Figure 4F; Additional file 1: Figure S3B).

TEM showed vesicle-like membranous structures in all four CMEV groups (Figure 4G). Tre-CMEVs had a narrower particle size distribution than Glc-CMEVs, while all four groups had negative zeta potentials (Figure 4C,D). The zeta potential of Tre-CMEVs was comparable to that of Glc-CMEVs, whereas Gal-CMEVs and Gly-CMEVs showed significant differences from Glc-CMEVs.

Across three independent batches for each carbon source, the coefficients of variation for protein concentration, particle size, and zeta potential ranged from 1.14% to 8.90%, indicating low variation between batches (Additional file 1: Tables S1 and S2). The three independently prepared Tre-CMEV batches also produced similar reductions in MDA in UVB-injured HaCaT cells (Additional file 1: Figure S4).

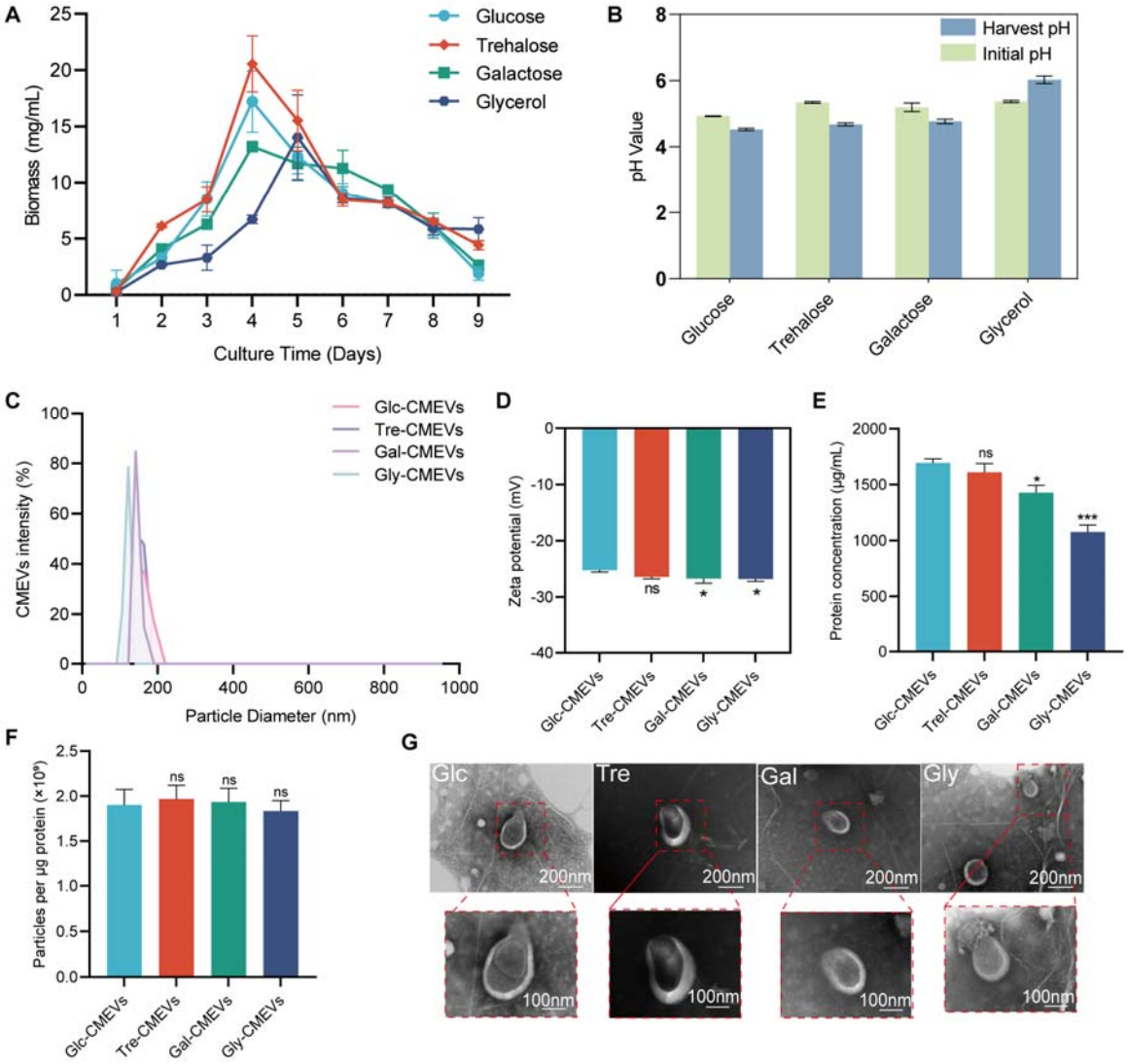


Figure 4. Effects of carbon source on CMEV characteristics. (A) Mycelial biomass during days 1-9 of submerged liquid fermentation with glucose (Glc), trehalose (Tre), galactose (Gal), or glycerol (Gly). (B) Initial broth pH and pH at the condition-specific peak-biomass collection point. (C) Intensity-weighted particle-size distributions. (D) Zeta potential. (E) BCA-measured protein concentration. (F) NTA-detectable particles per μg of BCA-measured protein. (G) Representative TEM images; upper scale bars, 200 nm; lower scale bars, 100 nm. Glc-CMEVs, Tre-CMEVs, and Gal-CMEVs were collected on fermentation day 4, whereas Gly-CMEVs were collected on day 5. Data are mean ± SD from three independent fermentation and complete preparation batches. Comparisons used one-way ANOVA with Dunnett's test against Glc-CMEVs. *$P < 0.05$, ***$P < 0.001$, ns, not significant.

3.4. Protective effects of CMEVs produced with different carbon sources in UVB-injured HaCaT cells

The protective effects of CMEVs produced with different carbon sources were evaluated in UVB-injured HaCaT cells. Compared with the UVB Model group, all four CMEV treatments reduced ROS and MDA levels, with Tre-CMEVs showing the lowest levels among the intervention groups (Figure 5A–C). All four treatments also decreased *IL-6* and *MMP-1* mRNA expression and increased *COL1A2* mRNA expression to varying degrees (Figure 5D–F). Tre-CMEVs showed the lowest ROS and MDA levels together with favorable changes in the three injury-related genes and were therefore selected for subsequent in vivo evaluation. Tre-CMEVs and Glc-CMEVs were used for the primary metabolomics comparison; comparisons involving Gal-CMEVs and Gly-CMEVs are presented in Additional file 1: Figure S6.

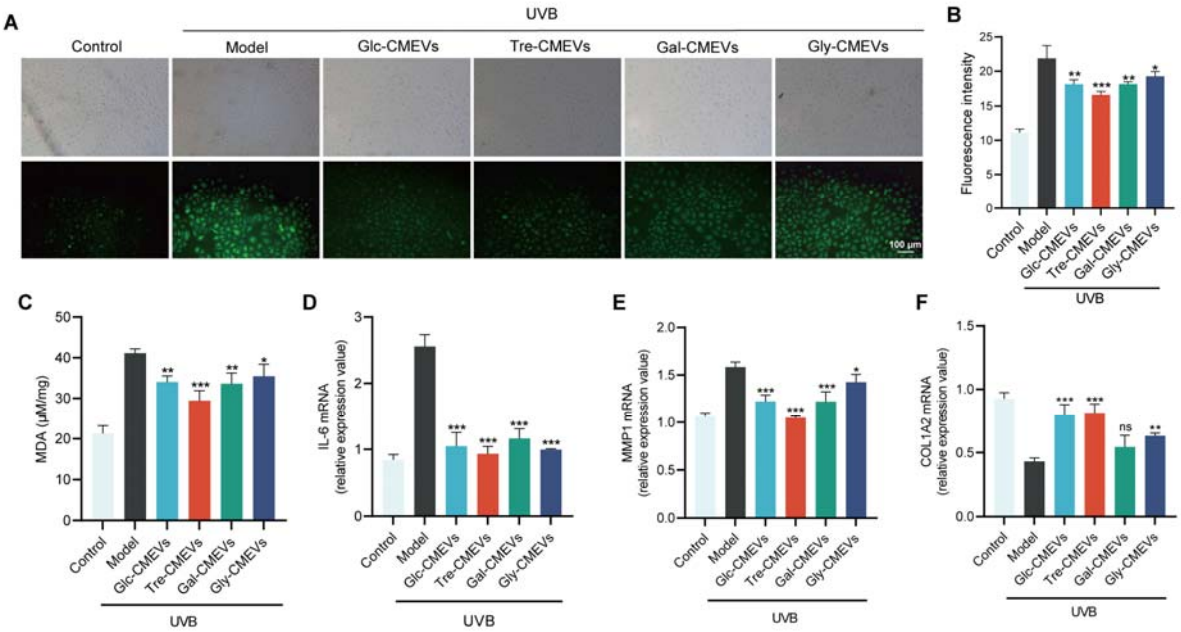


Figure 5. Protective effects of CMEVs produced with different carbon sources against UVB-induced HaCaT injury. (A) Representative bright-field and DCFH-DA fluorescence images showing intracellular ROS accumulation in the control, UVB Model, Glc-CMEVs, Tre-CMEVs, Gal-CMEVs, and Gly-CMEVs groups. (B) Quantification of relative intracellular ROS fluorescence intensity. (C) MDA concentration measured by a TBA-based assay. (D-F) Relative mRNA expression of *IL-6*, *MMP-1*, and *COL1A2*. Data are mean ± SD, n = 3. Comparisons were made between each CMEV intervention group and the Model group by one-way ANOVA with Dunnett's post hoc test; *$P < 0.05$, **$P < 0.01$, ***$P < 0.001$.

3.5. Untargeted metabolomics identifies differences between Tre-CMEVs and Glc-CMEVs

Untargeted LC-MS/MS identified differential features in several chemical subclasses, including amino acids and derivatives, flavonoids, and organic acids (Figure 6A). The OPLS-DA score plot separated Tre-CMEVs from Glc-CMEVs (Figure 6C), and the permutation test yielded a negative Q^2 regression intercept, indicating no obvious overfitting (Figure 6B). These results showed that Tre-CMEVs and Glc-CMEVs had distinct metabolite profiles.

The heat map showed different relative-abundance patterns between Tre-CMEVs and Glc-CMEVs (Figure 6D). Several features with higher abundance in Tre-CMEVs were putatively annotated as arginine, glutamate, and TCA cycle intermediates. KEGG analysis associated the differential features with amino acid metabolism, energy metabolism, and redox-related pathways (Figure 6E). These features were selected as candidates for subsequent targeted validation. Tre-CMEVs also separated from Gal-CMEVs and Gly-CMEVs in the OPLS-DA models, with corresponding differences observed in the heat maps (Additional file 1: Figure S6).

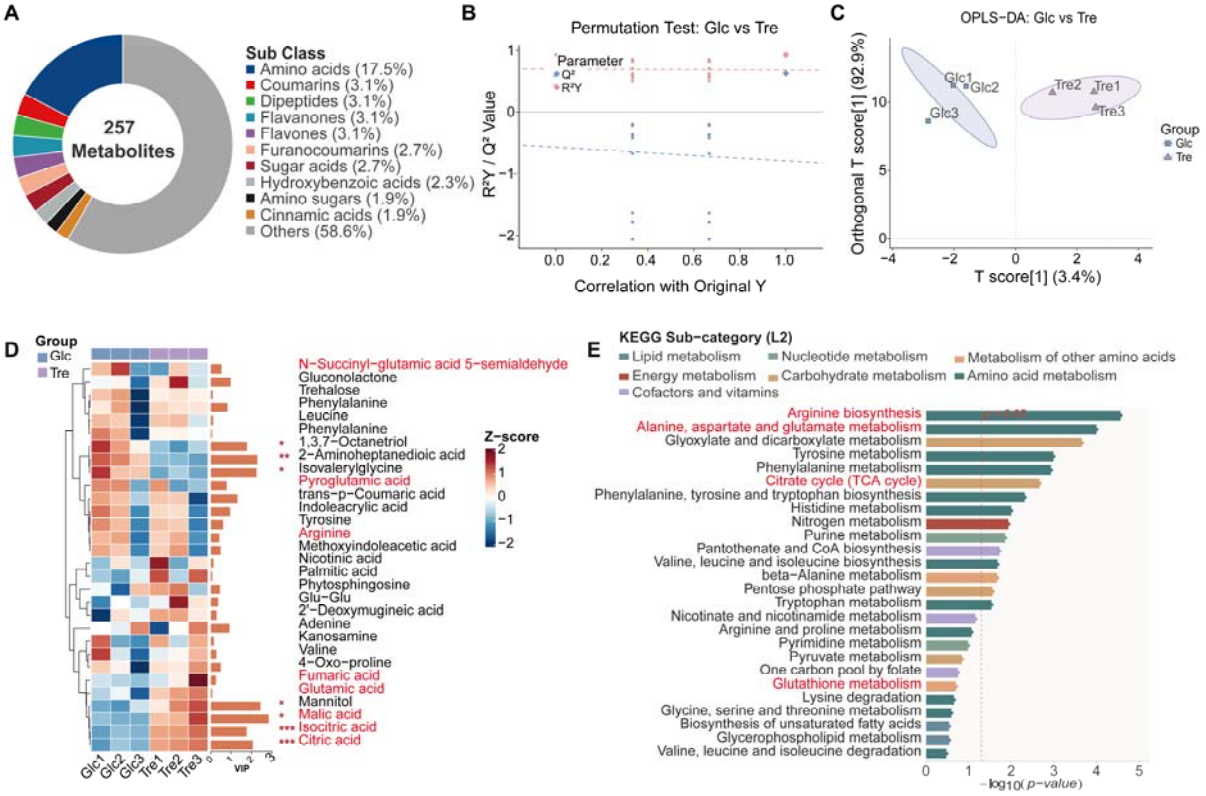


Figure 6. Untargeted metabolomics of Tre-CMEVs and Glc-CMEVs. (A) RefMet chemical subclass distribution of differential features. (B) OPLS-DA permutation test (n = 200); the negative Q^2 regression intercept indicated no obvious overfitting under the applied settings. (C) OPLS-DA score plot. (D) Heat map of the top 30 differential features; relatively elevated features in Tre-CMEVs included signals putatively annotated as arginine, glutamate, and TCA-cycle intermediates. (E) KEGG pathway mapping of differential features. Data were derived from three independent fermentation and complete preparation batches per group; differential-feature screening used VIP > 1.0 and Benjamini-Hochberg-adjusted $P < 0.05$.

3.6. Tre-CMEVs attenuate UVB-induced skin photoaging in mice

Following the in vitro carbon-source screening, Tre-CMEVs were evaluated in the mouse UVB model (Figure 7A). Repeated UVB exposure caused erythema, scaling, and deepened wrinkles in the UVB Model group. These changes were attenuated by Tre-CMEVs, and wrinkle severity scores were significantly lower than those in the UVB Model group (Figure 7B,D).

Histological findings were consistent with the macroscopic changes. H&E staining showed epidermal hyperplasia and abnormal keratinization in the UVB Model group, whereas treatment with Tre-CMEVs significantly reduced epidermal thickness (Figure 7C,E). Masson's trichrome staining showed disruption and loss of dermal collagen after UVB exposure. Treatment with Tre-CMEVs improved collagen organization and significantly increased the collagen area fraction (Figure 7C,F).

Treatment with Tre-CMEVs decreased *IL-1β* and *MMP1A* mRNA expression, increased *COL1A2* mRNA expression, and reduced MDA levels in UVB-damaged skin (Figure 7G–J). Together, these findings support a protective effect of Tre-CMEVs against the measured UVB-induced skin changes.

No obvious histopathological abnormalities were observed in the heart, liver, spleen, lung, kidney, or skin of Tre-CMEV-treated mice, and body weight remained stable during the observation period (Additional file 1: Figure S7). These findings indicated no obvious short-term toxicity under the tested conditions.

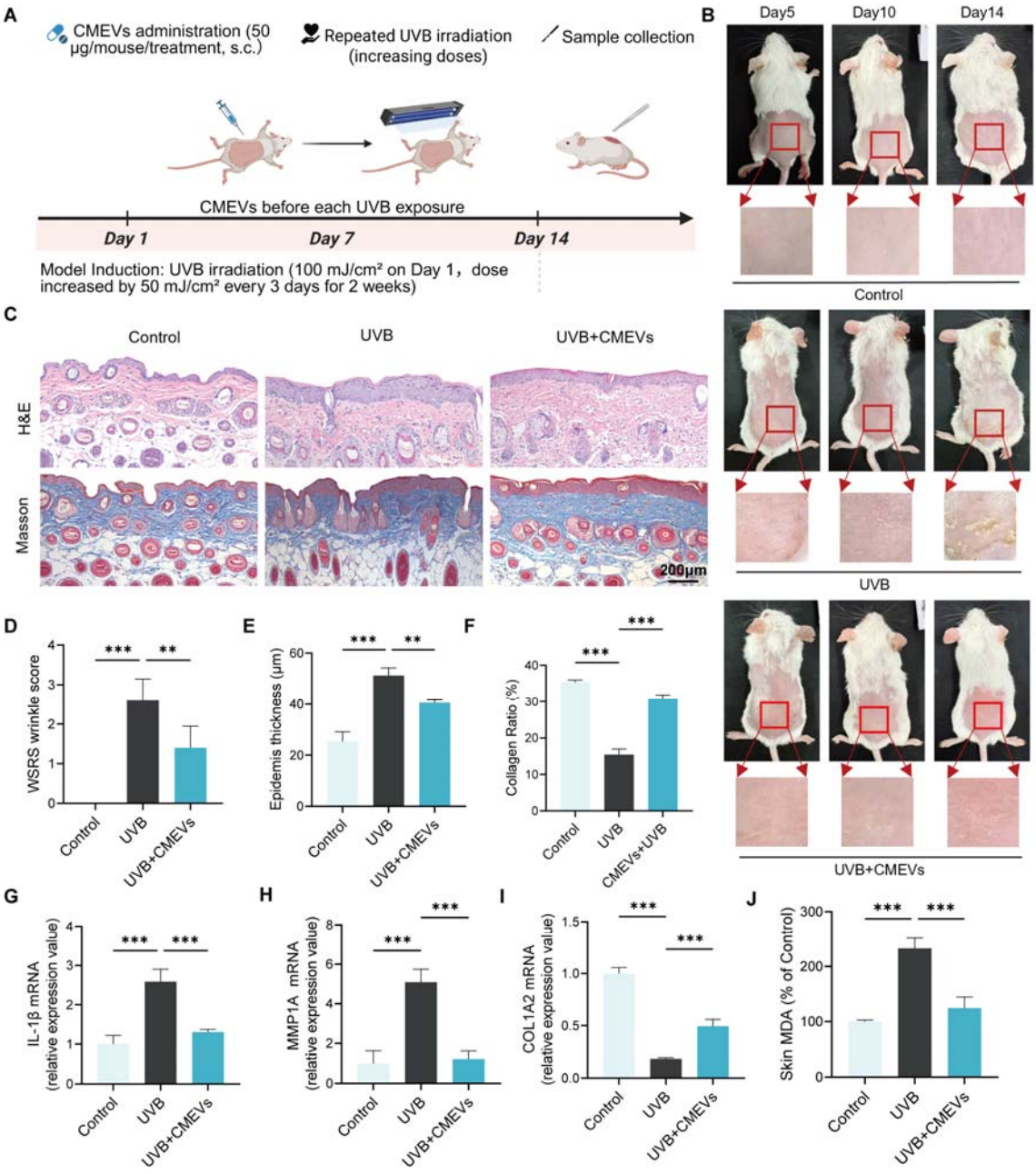


Figure 7. Tre-CMEVs attenuate UVB-induced skin photoaging relative to the UVB Model group. (A) Schematic of the 14-day UVB photoaging model and subcutaneous Tre-CMEVs intervention. (B) Macroscopic dorsal skin appearance and local magnified images on days 5, 10, and 14. (C) Representative H&E and Masson's trichrome staining; scale bar, 200 μm. (D) Wrinkle severity score. (E) Epidermal thickness. (F) Dermal collagen area fraction. (G-I) Relative mRNA expression of *IL-1β*, *MMP1A*, and *COL1A2* in dorsal skin. (J) Relative MDA level in skin homogenates. Data are mean ± SD, n = 6 mice per group. Comparisons used one-way ANOVA with Dunnett's test against the UVB Model group. $^{**}P < 0.01$, $^{***}P < 0.001$.

4. Discussion

This study showed that source material, collection time, and carbon source affected the physicochemical characteristics and UVB-protective activity of CMEVs. SF-CMEVs showed more uniform physicochemical characteristics than FB-CMEVs, fermentation day 4 provided a suitable collection time, and Tre-CMEVs consistently protected HaCaT cells and mouse skin against UVB-induced injury. These findings link the fermentation conditions to CMEV characteristics and biological activity.

Compared with FB-CMEVs, SF-CMEVs showed higher protein recovery per gram of source dry mass, a more negative zeta potential, and a narrower particle size distribution, while the particle-to-protein ratios were comparable between the two groups. These results suggest that submerged liquid fermentation produced CMEVs with more uniform physicochemical characteristics and provided greater control over the production conditions than fruiting-body extraction. However, dry fruiting-body material and dry mycelial biomass are not biologically equivalent denominators; therefore, the protein recovery results should be interpreted as an operational comparison rather than evidence of absolute source superiority.

Protein concentration was highest on fermentation day 5; however, CMEVs collected on day 5 had a lower particle-to-protein ratio and greater particle heterogeneity than those collected on day 4. CMEVs collected on day 4 also showed favorable particle characteristics and consistently reduced oxidative stress and injury-related gene expression in HaCaT cells. These results indicate that the collection time should be selected using particle characteristics and biological activity rather than total protein concentration alone. Fermentation day 4 was therefore selected for the subsequent experiments. Because the cell experiments used protein-normalized doses, differences in particle exposure may have partly contributed to the responses observed at different collection times.

Tre-CMEVs had protein concentration, particle-to-protein ratio, and zeta potential values comparable to those of Glc-CMEVs, but showed stronger protection against UVB-induced injury in HaCaT cells and a distinct metabolite profile. These findings suggest that changing the carbon source altered the biological properties and metabolic composition of CMEVs without causing a large change in their particle-to-protein ratio. Similar effects of culture conditions on small-molecule profiles have been reported in other food fermentation systems[48, 49]. However, residual carbon sources, osmotic conditions, cordycepin, and adenosine were not measured; therefore, the specific fermentation factors responsible for the observed differences remain unclear.

Tre-CMEVs consistently attenuated UVB-induced injury in both HaCaT cells and mice. In HaCaT cells, Tre-CMEVs reduced ROS and MDA levels, decreased *IL-6* and *MMP-1* mRNA expression, and increased *COL1A2* mRNA expression. In mice, Tre-CMEVs reduced wrinkle severity, epidermal hyperplasia, skin MDA, *IL-1β*, and *MMP1A* expression, while preserving dermal collagen and increasing *COL1A2* expression. Together, these results indicate that Tre-CMEVs alleviated oxidative stress and inflammatory responses and helped maintain collagen homeostasis during UVB-induced injury. Similar antioxidant and collagen-preserving effects have been reported for other food-associated microorganisms, peptides, and food-derived interventions[52, 53]. The observed changes are consistent with regulation of redox, inflammatory, and extracellular-matrix-related pathways, although the corresponding pathway proteins and phosphorylation states were not directly measured.

Untargeted metabolomics further showed that Tre-CMEVs and Glc-CMEVs had distinct metabolite profiles. Several features with higher abundance in Tre-CMEVs were putatively annotated as arginine, glutamate, and TCA cycle intermediates and were mainly associated with amino acid and energy metabolism.

This pattern suggests that trehalose altered the metabolic composition of CMEVs and provides a possible biochemical context for the stronger protective effects observed in HaCaT cells. However, because these annotations were not confirmed using authentic standards and their localization within CMEVs was not determined, no individual metabolite can yet be identified as the active component.

Submerged liquid fermentation enabled the carbon source, culture time, biomass, and broth pH to be monitored during CMEV production. The coefficients of variation for protein concentration, particle size, and zeta potential ranged from 1.14% to 8.90% across independent batches, and three Tre-CMEV batches produced similar reductions in MDA. These results indicate good repeatability under the tested conditions and support submerged liquid fermentation as a controllable platform for CMEV production. Further scale-up should evaluate bioreactor performance, downstream purification, DTT and PEG clearance, storage stability, and the additional cost associated with trehalose.

The comparable particle-to-protein ratios among the source and carbon-source groups indicate that the protein-normalized comparisons were unlikely to be dominated by large differences in particle exposure. More importantly, Tre-CMEVs protected against UVB-induced injury in both HaCaT cells and mice, supporting the biological relevance of the in vitro screening results. Nevertheless, particle-normalized functional experiments are still needed. Because the animal experiment did not include a Glc-CMEVs group, it demonstrates the in vivo protective activity of Tre-CMEVs but does not establish their superiority over Glc-CMEVs. In addition, the subcutaneous administration route and short observation period limit direct extrapolation to topical, oral, or food-related applications.

5. Conclusions

Under the tested submerged liquid fermentation conditions, source material, collection time, and carbon source affected CMEV characteristics and UVB-protective activity. Fermentation day 4 was selected as the collection time based on the particle characteristics and protective effects of the resulting CMEVs in HaCaT cells. Among the four carbon sources tested in vitro, Tre-CMEVs showed the most consistent protection against UVB-induced HaCaT cell injury. Tre-CMEVs also reduced wrinkles, epidermal thickening, oxidative damage, inflammatory responses, and collagen loss in UVB-exposed mice. Untargeted metabolomics revealed differences between Tre-CMEVs and Glc-CMEVs, particularly in features related to amino acid and energy metabolism. These findings support submerged liquid fermentation as a controllable approach for CMEV production and identify Tre-CMEVs as a candidate for further compositional and functional validation.

Supplementary material

Additional file 1. Supporting figures and tables. Figure S1 evaluates the DTT matrix-dissociation step. Figure S2 characterizes unconditioned fermentation-medium controls and the DTT treatment and PEG enrichment process blank. Figure S3 presents NTA-derived particle-concentration profiles and particle-to-protein ratios. Figure S4 evaluates functional consistency among three independently prepared

Tre-CMEV batches. Figure S5 presents the processed DiI-only control for the cellular-uptake experiment. Figure S6 provides auxiliary metabolomic comparisons of Tre-CMEVs with Gal-CMEVs and Gly-CMEVs. Figure S7 presents the preliminary in vivo tolerability assessment. Tables S1 and S2 summarize batch-to-batch reproducibility and individual batch measurements. Table S3 lists RT-qPCR primer sequences, and Table S4 lists reagents and instruments.

Availability of data and materials

The data supporting the findings of this study are included in the article and its supplementary information files. The underlying raw datasets are available from the corresponding author upon reasonable request.

Declaration

The authors declare that they have no known competing financial interests or personal relationships that could have appeared to influence the work reported in this paper.

The funding source is disclosed in the manuscript. The funder had no role in study design, data collection and analysis, data interpretation, manuscript preparation, or the decision to submit the article for publication.

References

[1] K.J. Jędrejko, J. Lazur, B. Muszyńska, Cordyceps militaris: An Overview of Its Chemical Constituents in Relation to Biological Activity, Foods. 10 (2021) 2634. https://doi.org/10.3390/foods10112634.

[2] A.-R. Phull, M. Ahmed, H.-J. Park, Cordyceps militaris as a Bio Functional Food Source: Pharmacological Potential, Anti-Inflammatory Actions and Related Molecular Mechanisms, Microorganisms. 10 (2022) 405. https://doi.org/10.3390/microorganisms10020405.

[3] H.-J. Park, Influence of Culture Conditions on Bioactive Compounds in Cordyceps militaris: A Comprehensive Review, Foods. 14 (2025) 3408. https://doi.org/10.3390/foods14193408.

[4] D. Kontogiannatos, G. Koutrotsios, S. Xekalaki, et al., Biomass and Cordycepin Production by the Medicinal Mushroom Cordyceps militaris—A Review of Various Aspects and Recent Trends towards the Exploitation of a Valuable Fungus, J. Fungi. 7 (2021) 986. https://doi.org/10.3390/jof7110986.

[5] Y. Chang, X. Liu, Y. Jiao, et al., Improved Cordycepin Production by Cordyceps Militaris Using Corn Steep Liquor Hydrolysate as an Alternative Protein Nitrogen Source, Foods. 13 (2024) 813. https://doi.org/10.3390/foods13050813.

[6] L. Wang, H. Yan, B. Zeng, et al., Research Progress on Cordycepin Synthesis and Methods for Enhancement of Cordycepin Production in Cordyceps militaris, Bioengineering. 9 (2022) 69. https://doi.org/10.3390/bioengineering9020069.

[7] A. Turk, M.A.A. Abdelhamid, S.W. Yeon, et al., Cordyceps mushroom with increased cordycepin content by the cultivation on edible insects, *Front. Microbiol.* 13, 1017576 (2022) https://doi.org/10.3389/fmicb.2022.1017576.

[8] X. Li, R. Jiang, S. Wang, et al., Prospects for cordycepin biosynthesis in microbial cell factories, *Front. Chem. Eng.* 6, 1446454 (2024) https://doi.org/10.3389/fceng.2024.1446454.

[9] J. Liang, M. Zhang, X. Li, et al., Structure and immunomodulatory activity of Lentinus edodes polysaccharides modified by probiotic fermentation, Food Science and Human Wellness. 13 (2024) 421-433. https://doi.org/10.26599/FSHW.2022.9250036.

[10] K.W. Lange, Y. Nakamura, Amazake (Japanese fermented rice beverage) and its potential health benefits, Food Science and Human Wellness. 14 (2025) 9250076. https://doi.org/10.26599/FSHW.2024.9250076.

[11] J.A. Welsh, D.C.I. Goberdhan, L. O'Driscoll, et al., Minimal information for studies of extracellular vesicles (MISEV2023): From basic to advanced approaches, Journal of Extracellular Vesicles. 13 (2024) e12404. https://doi.org/10.1002/jev2.12404.

[12] Y. Zhang, M. Lan, Y. Chen. Minimal Information for Studies of Extracellular Vesicles (MISEV): Ten-Year Evolution (2014–2023). *Pharmaceutics.* 16. 2024:1394. https://doi.org/10.3390/pharmaceutics16111394.

[13] C. Qiang, L. Halilovic, T. Shi, et al., Extracellular vesicles: cross-organismal RNA trafficking in plants, microbes, and mammalian cells, Extracell. Vesicles Circ. Nucleic Acids. 4 (2023) 262-282. https://doi.org/10.20517/evcna.2023.10.

[14] J. Rizzo, A. Taheraly, G. Janbon, Structure, composition and biological properties of fungal extracellular vesicles, microLife. 2, uqab009 (2021) https://doi.org/10.1093/femsml/uqab009.

[15] H.C. de Oliveira, A.F. Kato, B.A.G. Sena, et al. Biogenesis of Fungal Extracellular Vesicles: What Do We Know? In: Rodrigues M., G. Janbon, editors. *Fungal Extracellular Vesicles: Biological Roles*. Cham: Springer International Publishing; ,2021, p. 1-11. https://doi.org/10.1007/978-3-030-83391-6_1.

[16] Y. Lai, B. Jiang, F. Hou, et al., The emerging role of extracellular vesicles in fungi: a double-edged sword, *Front. Microbiol.* 14, 1216895 (2023) https://doi.org/10.3389/fmicb.2023.1216895.

[17] K.-J. Lo, M.-H. Wang, C.-T. Ho, et al., Plant-Derived Extracellular Vesicles: A New Revolutionization of Modern Healthy Diets and Biomedical Applications, *J. Agric. Food Chem.* 72 (2024) 2853-2878. https://doi.org/10.1021/acs.jafc.3c06867.

[18] Q. Jiang, L. Wang, J. Tian, et al., Food-derived extracellular vesicles: natural nanocarriers for active phytoconstituents in new functional food, Crit. Rev. Food Sci. Nutr. 64 (2024) 11701-11721. https://doi.org/10.1080/10408398.2023.2242947.

[19] J. Kim, S. Li, S. Zhang, et al., Plant-derived exosome-like nanoparticles and their therapeutic activities, Asian J. Pharm. Sci. 17 (2022) 53-69. https://doi.org/10.1016/j.ajps.2021.05.006.

[20] B. Zhao, H. Lin, X. Jiang, et al., Exosome-like nanoparticles derived from fruits, vegetables, and herbs: innovative strategies of therapeutic and drug delivery, Theranostics. 14 (2024) 4598-4621. https://doi.org/10.7150/thno.97096.

[21] R. Liu, F. Zhang, X. He, et al., Plant Derived Exosome-Like Nanoparticles and Their Therapeutic Applications in Glucolipid Metabolism Diseases, *J. Agric. Food Chem.* 73 (2025) 6385-6399. https://doi.org/10.1021/acs.jafc.4c12480.

[22] J. Cheng, Y. Zhu, Review on extraction technology and function of plant-derived exosome-like nanoparticles, *Front. Med. Technol.* 7, 1668738 (2025) https://doi.org/10.3389/fmedt.2025.1668738.

[23] X. Lu, Q. Han, J. Chen, et al., Celery (Apium graveolens L.) Exosome-like Nanovesicles as a New-Generation Chemotherapy Drug Delivery Platform against Tumor Proliferation, J. Agric. Food Chem. 71 (2023) 8413-8424. https://doi.org/10.1021/acs.jafc.2c07760.

[24] X. Yang, Z. Zong, B. Niu, et al., Shiitake mushroom-derived extracellular nanovesicles: Preparation, characterization, and inhibition of Caco-2 cells, Food Chem. 463 (2025) 141339. https://doi.org/10.1016/j.foodchem.2024.141339.

[25] X. Li, B. Liu, D. Sekar, et al., Shiitake Mushroom-Derived Vesicle-like Nanoparticles Improve Cognitive Function and Reshape Gut Microbiota and Fecal Metabolome in Aged Mice, Nutrients. 17 (2025) 2902. https://doi.org/10.3390/nu17172902.

[26] G. Cusumano, A. Bertoldi, E. Calzoni, et al., Therapeutic Potential of Bioactive Compounds in Edible Mushroom-Derived Extracellular Vesicles: Isolation and Characterization of EVs from Pleurotus eryngii, Pharmaceuticals. 18 (2025) 1362. https://doi.org/10.3390/ph18091362.

[27] J. Han, T. Wu, J. Jin, et al., Exosome-like nanovesicles derived from Phellinus linteus inhibit Mical2 expression through cross-kingdom regulation and inhibit ultraviolet-induced skin aging, *J. Nanobiotechnol.* 20 (2022) 455. https://doi.org/10.1186/s12951-022-01657-6.

[28] H. Liu, T. Dong, C. Dong, et al., Plant-derived exosome-like nanovesicles: a novel therapeutic perspective for skin diseases, *J. Nanobiotechnol.* 23 (2025) 640. https://doi.org/10.1186/s12951-025-03715-1.

[29] W. Wei, X. Ren, F. Yi, et al., Innovative Plant Exosome Delivery System for Enhancing Antiaging Potency on Skin, *ACS Appl. Bio Mater.* 8 (2025) 2117-2127. https://doi.org/10.1021/acsabm.4c01691.

[30] D.A. Salgado-Bautista, M. Riquelme, Growth conditions shape the proteome and diversity of Neurospora crassa extracellular vesicles, Cell Surf. 14 (2025) 100152. https://doi.org/10.1016/j.tcsw.2025.100152.

[31] G.D. Ribeiro, L. de Holanda Paranhos, E.C.A. Eleutherio, Trehalose promotes biological fitness of fungi, Fungal Biol. 128 (2024) 2381-2389. https://doi.org/10.1016/j.funbio.2024.03.004.

[32] Y. Liu, B. Li, T. Chen, et al., The synthesis, degradation and biological function of trehalose-6-phosphate, Stress Biol. 5 (2025) 38. https://doi.org/10.1007/s44154-025-00235-8.

[33] Y. Luo, X. Ou, D. Liu, et al., A novel exosome-like nanovesicles from Cordyceps militaris potentiate immunomodulatory and anti-tumor effect by reprogramming macrophages, Life Sci. 358 (2024) 123163. https://doi.org/10.1016/j.lfs.2024.123163.

[34] N.P. du Sert, V. Hurst, A. Ahluwalia, et al., The ARRIVE guidelines 2.0: Updated guidelines for reporting animal research, PLOS Biology. 18 (2020) e3000410. https://doi.org/10.1371/journal.pbio.3000410.

[35] P. Fernández-Llama, S. Khositseth, P.A. Gonzales, et al., Tamm-Horsfall protein and urinary exosome isolation, Kidney International. 77 (2010) 736-742. https://doi.org/10.1038/ki.2009.550.

[36] S. Williams, M. Fernandez-Rhodes, A. Law, et al., Comparison of extracellular vesicle isolation processes for therapeutic applications, J. Tissue Eng. 14 (2023) 20417314231174609. https://doi.org/10.1177/20417314231174609.

[37] T. Liangsupree, E. Multia, M.-L. Riekkola, Recent advances in modern extracellular vesicle isolation and separation techniques, J. Chromatogr. A. 1767 (2026) 466602. https://doi.org/10.1016/j.chroma.2025.466602.

[38]L. Ni, Y. Zou, Z. Zhu, Guideline for the Extraction of Extracellular Vesicles From Edible Plants, Fungi and Bacteria, AgriFood: Journal of Agricultural Products for Food. 1 (2025) 31-40. https://doi.org/10.1002/agf2.70004.

[39] G. Kowkabany, Y. Bao, Nanoparticle Tracking Analysis: An Effective Tool to Characterize Extracellular Vesicles, Molecules. 29 (2024) 4672. https://doi.org/10.3390/molecules29194672.

[40]F. Papaccio, A. D′Arino, S. Caputo, et al., Focus on the Contribution of Oxidative Stress in Skin Aging, Antioxidants. 11 (2022) 1121. https://doi.org/10.3390/antiox11061121.

[41] T. Tong, R. Geng, S.-G. Kang, et al., Revitalizing Photoaging Skin through Eugenol in UVB-Exposed Hairless Mice: Mechanistic Insights from Integrated Multi-Omics, Antioxidants. 13 (2024) 168. https://doi.org/10.3390/antiox13020168.

[42] J. Wang, M. Yuan, Q. Li, et al., Combined protection against UVB-induced photoaging by oleuropein, hydroxytyrosol, and verbascoside through modulation of inflammation, oxidative stress, and collagen homeostasis, Sci. Rep. 15 (2025) 41008. https://doi.org/10.1038/s41598-025-24845-4.

[43] G. Li, T. Jian, X. Liu, et al. Application of Metabolomics in Fungal Research. *Molecules.* 27. 2022:7365. https://doi.org/10.3390/molecules27217365.

[44] E. Fahy, S. Subramaniam, RefMet: a reference nomenclature for metabolomics, Nature Methods. 17 (2020) 1173-1174. https://doi.org/10.1038/s41592-020-01009-y.

[45] M. Kanehisa, M. Furumichi, Y. Sato, et al., KEGG for taxonomy-based analysis of pathways and genomes, Nucleic Acids Res. 51 (2023) D587-D592. https://doi.org/10.1093/nar/gkac963.

[46] L.W. Sumner, A. Amberg, D. Barrett, et al., Proposed minimum reporting standards for chemical analysis: Chemical Analysis Working Group (CAWG) Metabolomics Standards Initiative (MSI), Metabolomics. 3 (2007) 211-221. https://doi.org/10.1007/s11306-007-0082-2.

[47] C. Zhao, S. Wu, H. Wang, Medicinal Plant Extracts Targeting UV-Induced Skin Damage: Molecular Mechanisms and Therapeutic Potential, Int. J. Mol. Sci. 26 (2025) 2278. https://doi.org/10.3390/ijms26052278.

[48] T. Lan, Q. Zhao, J. Wang, et al., Widely targeted metabolomics analysis of the effects of probiotic fermentation on the phytochemicals of kiwifruit juice and prediction of key metabolic pathways, Food Science and Human Wellness. 14 (2025) 9250257. https://doi.org/10.26599/FSHW.2024.9250257.

[49] J. Wang, S. Mei, C. Jin, et al., Discovery of taste-active metabolites in Lactobacillus plantarum-fermented chili sauce via web-based computational analysis, Food Science and Human Wellness. 14 (2025) 9250048. https://doi.org/10.26599/FSHW.2024.9250048.

[50] H. Nie, X. Ma, F. Kong, et al., Improvement of Lactiplantibacillus plantarum MWFLp-182 on oxidative deficits induced by in 2,2'-azobis(2-methylpropionamidine) dihydrochloride and the relating key gene analysis, Food Science and Human Wellness. 14 (2025) 9250026. https://doi.org/10.26599/FSHW.2024.9250026.

[51] C. Li, L. Li, J. Cheng, et al., Antioxidant peptides from Lateolabrax japonicus to protect against oxidative stress injury in Drosophila melanogaster via biochemical and gut microbiota interaction assays, Food Science and Human Wellness. 14 (2025) 9250154. https://doi.org/10.26599/FSHW.2024.9250154.

[52] J. Tian, J. Liao, B. Zhong, et al., Anti-skin-aging effect of fish gelatin from Cynoscion acoupa by maintaining collagen matrix homeostasis on D-galactose induced aging mice, Food Science and Human Wellness. 14 (2025) 9250179. https://doi.org/10.26599/FSHW.2024.9250179.

[53] Y. Xia, Y. Gong, X. Lin, et al., Lactobacillus plantarum AR113 attenuates liver injury in D-galactose-induced aging mice via the inhibition of oxidative stress and endoplasmic reticulum stress, Food Science and Human Wellness. 13 (2024) 885-897. https://doi.org/10.26599/FSHW.2022.9250076.